PAPER

Check for updates

Performances of dual carbon multi-ion supercapacitors in aqueous and non-aqueous electrolytes†

Rachana Raavi, [iD] [a] Suresh Archana, [iD] [a] Pattubala Adinarayana Reddy[b] and Perumal Elumalai [iD] *[a]

Avocado-seed biomass-derived activated carbon was successfully synthesized by carbonization followed by chemical activation. The synthesized carbon was characterized using various material characterization techniques. The characterization data revealed that the carbon was porous with self-doped heteroatoms. The electrochemical characterizations confirmed that the carbon generated was capable of charge storage, exhibiting a high specific capacitance of 774 F g^{-1} at a current density of 0.7 A g^{-1} in the three-electrode cell. The detailed Dunn's method revealed that the charge storage is dominated by the capacitive mode. An aqueous supercapacitor fabricated in the form of the CR-2032 coin cell delivered a specific energy of 21 W h kg^{-1} at a specific power of 275 W kg^{-1}. For the first time, a dual carbon sodium-ion capacitor (DC-NIC) was fabricated using the avocado seed-derived carbon (AVAC) that exhibited outstanding specific energy of 72.36 W h kg^{-1} at a specific power of 320 W kg^{-1}, while a dual carbon lithium-ion capacitor (DC-LIC) device exhibited high specific energy of 55.25 W h kg^{-1} at a specific power of 300 W kg^{-1} with nearly 100% coulombic efficiency. The fabricated coin cell DC-NIC prototype was demonstrated to power commercial red, green, and blue LED bulbs. The once-charged DC-NIC coin cell could power the commercial green LED bulb for about 16 min.

1. Introduction

Carbon-based fossil fuels continue to be the primary source of various energy needs. The combustion of fossil fuels leads to an increased CO_2 emission on one hand and the reserves for such fossil fuels are being depleted on the other hand.[1,2] As a consequence, the emissions result in an adverse effect on the environmental ecosystem, which forces us to move towards the use of clean and green renewable energy resources such as solar, wind, and tidal.[3] As renewable energy sources are highly intermittent, it is essential to develop efficient energy storage devices.[4] In this regard, the electrochemical energy storage devices seem attractive. They are of two types, *viz.*, supercapacitors (supercaps) and batteries. Among the secondary batteries, lithium-ion batteries (LIBs) offer practically high specific energy (150–200 W h kg^{-1}) and coulombic efficiency

but suffer from limited specific power and cycle life.[5,6] On the other hand, supercaps are considered power devices, capable of fast charge/discharge with exceedingly high cycle life.[7] Due to instant charge/discharge, supercaps find their extensive use where a power surge is demanded. Based on the charge storage mechanisms, the supercaps are classified into electrical double-layer capacitors (EDLCs), which work on the basis of the charge separation at the electrode/electrolyte interface, and pseudo-capacitors, which involve a definite faradaic process. The supercaps can be further classified into symmetric capacitors and hybrid capacitors. A typical symmetric capacitor uses two identical electrodes, whereas, an asymmetric capacitor consists of two dissimilar electrodes.[8] Relatively, a modern device is being proposed with the aim to enhance specific energy of supercaps. Such modern devices are called metal-ion capacitors (MICs). Depending on the nature of the ion transportation between the positive and negative electrodes in the MIC, they are lithium-ion capacitor (LIC), sodium-ion capacitor (NIC), potassium-ion capacitor (KIC), *etc.*[9,10]

The most common materials used in the MICs are metal oxides, which are scarce, expensive, and have poor conductivity and poor cycling stability, leading to the almost impractical device.[11] An immediate option to overcome these issues is to use the earth's abundant carbonaceous material as an active

[a] *Electrochemical Energy Storage Lab, Department of Green Energy Technology, Madanjeet School of Green Energy Technologies, Pondicherry University, Puducherry – 605014, India. E-mail: drperumalelumalai@gmail.com, drperumalelumalai@pondiuni.ac.in; Tel: +91-413-2654867*

[b] *Evergreen Recylekaro India Pvt. Ltd., Millenium Business Park, Navi Mumbai – 400 701, India*

† Electronic supplementary information (ESI) available. See DOI: https://doi.org/10.1039/d2ya00271j

electrode instead of the expensive metal oxides. The carbon can be derived from any carbon-containing feedstock, such as aromatic compounds, cellulose, starch, and a variety of biomasses. Among them, the carbon derived from biomass is considered to be environmentally benign and facile. The biomass-derived carbons were used in various applications, such as dye adsorption, and battery anode.[12] Recent developments have been made on the dual carbon MIC, where the devices constitute two identical electrodes in aqueous or non-aqueous electrolytes. For example, Qian et al., fabricated a DC-LIC using the porous carbon flakes, which were derived from human hair that showed specific energy of 45.33 W h kg^{-1} at a specific power of 100 W kg^{-1}.[13] Similar work was done by Kesavan et al., using the Indian cake rusk (ICR) by means of pyrolysis followed by KOH activation that exhibited specific energy of 47.1 W h kg^{-1} at a specific power of 22 644 W kg^{-1}.[14] Recently, sodium-ion capacitors (NIC) are emerging as an attractive alternative to the DC-LIC. This is because lithium-based salts are becoming expensive due to scarcity as well as uneven distribution of the lithium reserves on the earth.[15] The NIC can also be constructed similarly to LIC. Hence, the biomass-derived carbon can serve as a good candidate for the NIC too, the resultant device can be a dual carbon sodium-ion capacitor (DC-NIC).[16] For example, Wang et al., developed a DC-NIC using the carbon derived from the peanut skin by means of carbonization that exhibited specific energy of 112 W h kg^{-1} at a low specific power of 67 W kg^{-1}.[17] Vadivazhagan et al., using corn silk-derived carbon reported specific energy of 109 W h kg^{-1} at a specific power of 12.16 W kg^{-1}.[18] Yin et al., developed the carbon from sugar using a hydrothermal process followed by chemical activation that exhibited specific energy of 43 W h kg^{-1} at a specific power of 3724 W kg^{-1}.[19]

The above studies revealed that the carbon-containing each biomass is unique, and so are the generated activated carbons. The electrode material is a key component for the good performance of the supercapacitors, which depends on the surface area, porosity, and conductivity of the active electrode material. The porous carbon can provide multidimensional electron transport pathways, easy access to the electrolyte, and minimize the transport distance between the grains, hence it can serve as a good candidate. The chemical activation offers the possibility of intentional heteroatom doping, which can lead to enhanced conductivity and redox properties of the resultant carbon. Hence, this work is focused on the generation of activated carbon from the avocado seed biomass waste through a simple pyrolysis method. The avocado seed is rich in carbon content, not edible, and widely available. To the best of our knowledge, there are no reports on the dual carbon sodium-ion and lithium-ion capacitors prepared using the avocado seed biomass-derived activated carbon in aqueous and non-aqueous electrolytes. Thus, detailed material generation, characterization, and device performances are reported here.

2. Experimental section

2.1. Material synthesis

The avocado seed biomass waste was collected from the Pondicherry University campus, crushed into small pieces, and dried in the sunlight for two days. The dried biomass (50 g) was pre-carbonized at 400 °C for 2 h in a muffle furnace in the air. The resultant biochar carbon was ground into a fine powder using a pestle and mortar. Then, 3 g pre-carbonized material was homogeneously mixed with 9 g KOH in a 1 : 3 ratio in 30 mL distilled water (DW) and stirred overnight. The volume of the water was allowed to be reduced by heating it at 100 °C. The resultant residue was finely ground and subjected to chemical activation at 800 °C for 1 h in a tubular furnace in an Argon atmosphere. The obtained product was thoroughly washed with dilute hydrochloric acid followed by DW until the filtrate pH reached a neutral value. Finally, the formed activated carbon was dried in a vacuum at 60 °C, overnight. The different stages involved in the generation of the activated carbon from the avocado seed biomass are shown in Scheme 1. The activated carbon derived from the avocado seed biomass is termed hereafter as AVAC.

2.2. Material characterization

The X-ray diffraction (XRD) pattern for the obtained AVAC was recorded in the 2θ range of 10–70° at a scan rate of 1° per min using a diffractometer (Bruker D8 XRD) equipped with a CuKα ($\lambda = 1.5184$ Å) radiation source. Fourier-transformed infrared (FT–IR) spectra were recorded (Nicolet 6700) using the KBr pellet method. Raman spectra were acquired using a Raman instrument (Witec Confocal) with a 718 nm Ar laser. The surface textural features were analyzed using scanning electron microscopy (Hitachi, S – 3400 N). X-ray photoelectron spectroscopy (XPS) analysis was performed (Thermo Scientific ESCALAB 250Xi) to find out the chemical state of the elements in the AVAC sample. The surface area and the pore size distribution of the sample were examined by the Brunaer–Emmett–Teller (BET) technique using N$_2$ as the adsorbing gas (NOVA touch 4LX).

2.3. Electrochemical characterizations

The electrochemical activity of the AVAC sample was tested initially in a three-electrode cell that consisted of AVAC on the carbon cloth as the working electrode, platinum (Pt) (1×1 cm^2) as the counter electrode, and Ag/AgCl as the reference electrode.
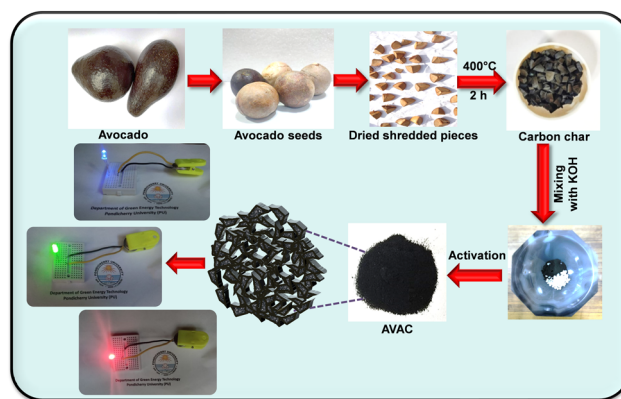
Scheme 1 Schematics of the various steps involved in the generation of the activated carbon from the avocado seed biomass.

The working electrode slurry was prepared by the homogeneous mixing of the active material (AVAC), super P carbon, and poly (vinylidene fluoride) (PVDF) binder in the weight ratio (wt%) 70 : 20 : 10 using N-methyl-2-pyrrolidone (NMP) as the solvent. The obtained slurry was coated on the carbon cloth current collector and dried overnight at 80 °C. The mass loading of the active material was 1.8 mg cm^{-2}. The three-electrode cell was subjected to cyclic voltammetry (CV) and the galvanostatic charge–discharge (GCD) studies in 1 M KOH were performed using an electrochemical workstation (Biologics, SP – 150). A laboratory proto-type supercapacitor device in the form of a CR-2032-type coin cell was fabricated using the AVAC as both positive and negative electrodes. 1 M KOH as the electrolyte and Whatman filter paper (150 mm) as a separator was used. The active material-coated carbon cloth was made into (16 mm diameter) discs and used as positive and negative electrodes for a symmetric device (AVAC|1 M KOH|AVAC). The performances of the dual carbon lithium-ion capacitor (DC-LIC) and the dual carbon sodium-ion capacitor (DC-NIC) were studied in 1 M LiPF$_6$ and 1 M NaClO$_4$ in EC/DEC (1 : 1 volume ratio), respectively. For the DC-LIC device, a Whatman filter paper (19 mm diameter) disc was used as a separator and for the DC-NIC device, a glass fiber separator was used. The CV, GCD, and cycle life profiles were recorded in the potential window of 0–1.1 V for the aqueous supercapacitor, 0–3 V for the DC-LIC, and 0–3.2 V for the DC-NIC at different scan rates or current rates using the same electrochemical workstation.

3. Results and discussion

The XRD patterns recorded for the avocado seed biomass-derived AVAC sample are shown in Fig. 1(a). The pattern has a broad Bragg peak at a diffraction angle of 20.1°, 2θ, and a weak peak at 43.5°. These sest of Bragg peaks are indexed to (002) and (100) planes of the carbon as per the standard pattern (Joint Committee on Powder Diffraction Standards (JCPDF No. 75–1621). The appearance of the broad peaks and the absence of the (101) and (004) peaks imply that the carbon formed is poorly crystalline and highly disordered. Further, the AVAC sample was subjected to Raman and FT-IR analyses. The presence of the defect and degree of the graphitization in the AVAC sample were examined using Raman spectroscopy. Fig. 1(b) shows the Raman profile recorded for the AVAC sample. Two Raman shifts centered at 1303 and 1585 cm^{-1} are observed, and these are attributed to D and G bands of the amorphous carbon sp^2 state. The G band arises due to the graphitic plane of the carbon layer stacking, whereas the defect associated with the carbon layers is seen as the D band. The band intensity ratio (I_D/I_G) computed was as high as 1.35, which revealed the presence of defects in the AVAC sample.[20] This is because at a high activation temperature, the following reaction occurred that resulted in more defects leading to an increased (I_D/I_G) ratio:

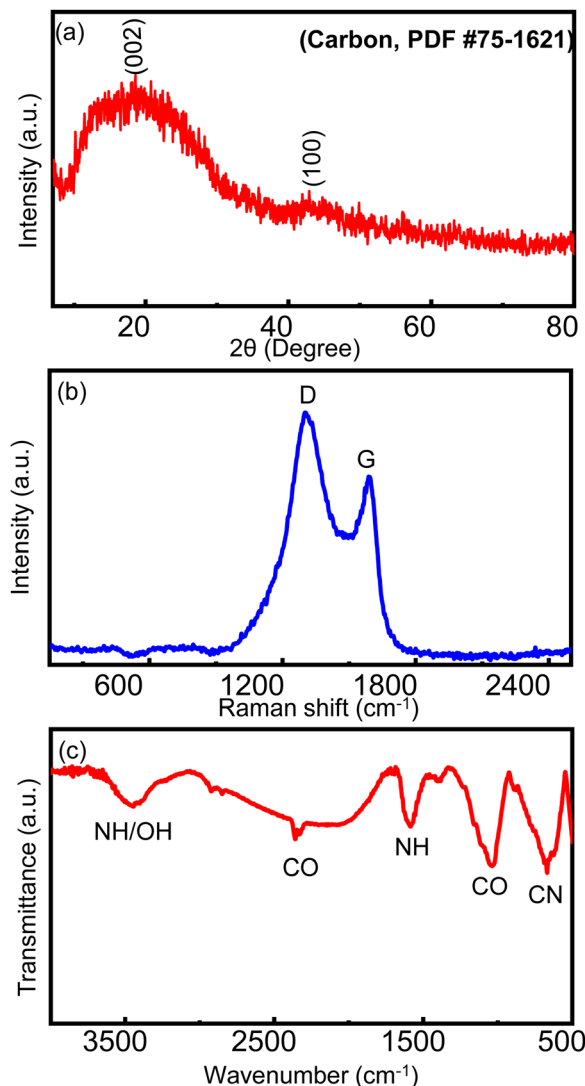$$2KOH + C \rightarrow CO_2 + K_2O + H_2O \tag{1}$$

Fig. 1 (a) XRD pattern, (b) Raman spectrum, and (c) FT-IR spectrum recorded for the avocado seed biomass-derived activated carbon.

The crystallite size of the AVAC was calculated from the Raman peaks using the following eq.:

$$L = (2.4 \times 10^{-10})\lambda^4(I_D/I_G)^{-1} \text{ nm} \tag{2}$$

where L is the average crystallite size, λ is the laser beam wavelength, and (I_D/I_G) is the band intensity ratio.[21] The crystallite size estimated was 45.67 nm. The FT-IR spectrum for the AVAC sample shown in Fig. 1(c) indicated bands at 3444, 2358, 1585, 1037, and 668 cm^{-1}, which are assigned to O–H/N–H, C=O, N–H, C–O, and C–N bonds, respectively.[22,23] Thus, the aforementioned XRD, Raman, and FT-IR results confirm that the avocado seed biomass-derived activated carbon is poorly crystalline and more disordered.

To examine the surface morphology of the AVAC sample, SEM analysis was done. The obtained representative SEM image is shown in Fig. 2(a). It is seen that the surface of the AVAC sample has grains and hierarchical pores. The grains were in the size range of 5–40 μm. Large pores are also seen on
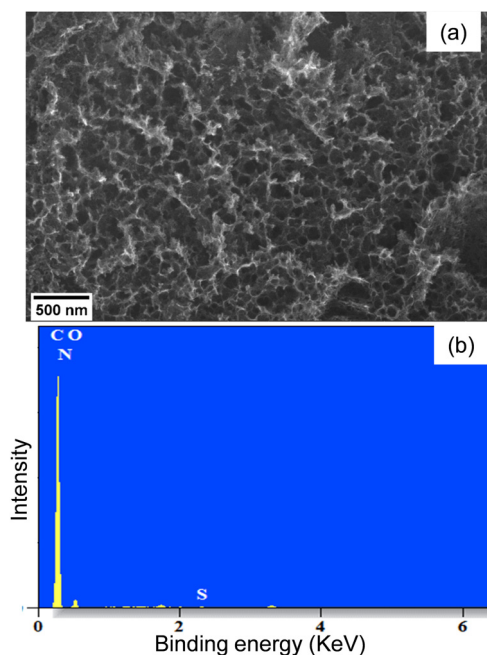
Fig. 2 (a) SEM image recorded (b) EDAX profile observed on the surface of the avocado seed biomass-derived carbon.

the matrix, which is formed during the chemical activation. The presence of such pores is expected to result in a high surface area and provide smoother ion transportation that may lead to better charge storage. Fig. 2(b) shows the energy dispersive

analysis of the X-ray (EDAX profile) recorded for the AVAC sample.

Furthermore, the presence of elements and their chemical states in the AVAC sample was determined using XPS analysis. The obtained XPS spectra of the AVAC sample are shown in Fig. 3(a–d) along with the survey spectrum. Fig. 3(a) shows the XPS survey spectrum recorded for the AVAC sample in the binding energy range of 0–1300 eV. The survey spectrum confirms the presence of the C, N, and O elements in the sample. Specifically, the binding energy peaks at 532.3, 420.5, and 284 eV correspond to the O 1s, N 1s, and C 1s, respectively. From the peak intensity, the amounts of carbon, oxygen, and nitrogen are 87.17%, 11.78%, and 1.04%, respectively. To get insights into the chemical states of the elements, the deconvoluted-Gaussian fitting was performed on the high-resolution spectrum of the C 1s, N 1s, and O 1s scans. Fig. 3(b) shows the deconvoluted C 1s scan profile, which consists of three significant binding energy peaks. The peaks present at the binding energies of 284.7, 285.4, 286.3, and 288.5 eV correspond to C–C, C–N, C–O, and C=O, respectively.[24] Fig. 3(c) shows the deconvoluted N 1s scan profile. It is observed that peaks are present in the range of 390–410 eV, which confirmed the presence of nitrogen in the AVAC sample. The N 1s scan profile is deconvoluted into four binding energy peaks centered at 398.6, 400.2, 401.3, and 402.8 eV, which correspond to pyridinic, pyrrolic, graphitic, and oxidized nitrogen, respectively.[25] The deconvoluted O 1s scan profile consists of three significant peaks, as shown in Fig. 3(d). The predominant peaks at binding energies
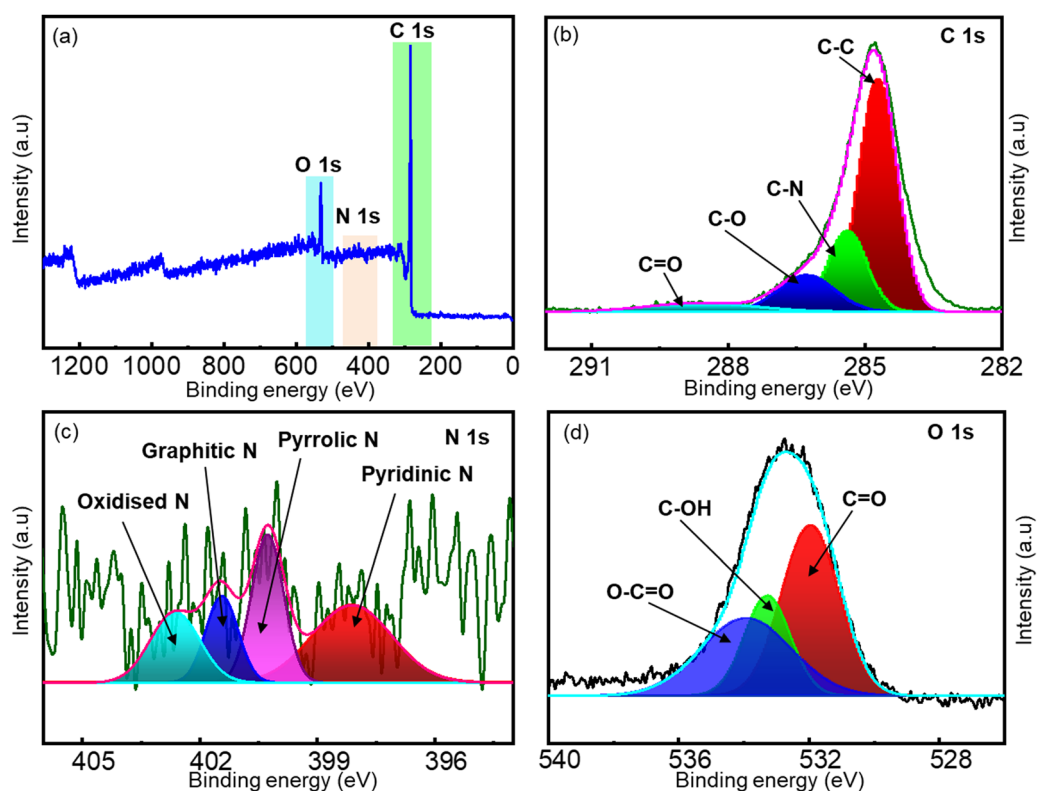

Fig. 3 (a) XPS survey spectrum and (b–d) deconvoluted scan profiles of C 1s, N 1s, and O 1s peaks recorded for the AVAC sample.
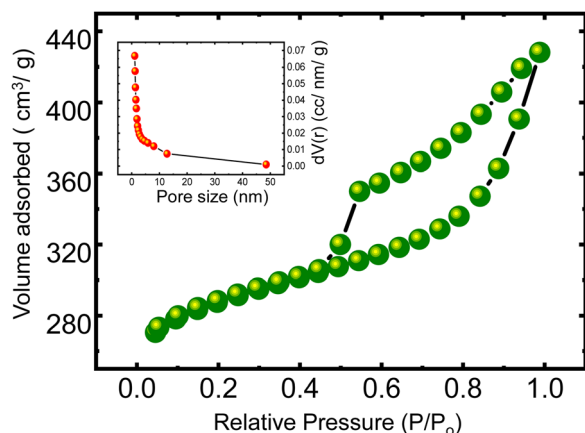
Fig. 4 N$_2$ adsorption–desorption isotherm curve. Inset: BJH pore size distribution recorded for the AVAC sample.

532.0, 533.4, and 534.7 eV correspond to C=O, C–OH, and O–C=O, respectively.[26] Thus, XPS results confirm that the AVAC sample is inherently doped with heteroatoms, such as nitrogen and oxygen, which can result in enhanced conductivity and better charge storage.

The surface area and pore size distribution of the AVAC sample were analyzed by the BET method. Fig. 4 shows the obtained adsorption isotherm. The adsorption follows Type-IV isotherm. The appearance of hysteresis at the high relative pressure (P/P_o) implies that the AVAC has mostly micropores

and few mesopores. Furthermore, the Barrett–Joyner–Halenda (BJH) pore size distribution in the inset of Fig. 4 clearly indicates the presence of micropores in the range of 0–2 nm radius in the AVAC sample. Only a few pores are in the higher radius. Interestingly, the AVAC exhibits a high surface area of 889.5 m^2 g^{-1} with a total pore volume of 0.66 cc g^{-1}. It should be noted that the chemical activation was performed using KOH as an activating agent, which resulted in such a porous structure. These pores are expected to improve ion diffusion, which is essential for high-charge storage.

3.1. Electrochemical activity of AVAC in a three-electrode cell

A three-electrode cell was initially fabricated to examine the charge storage features of the AVAC electrode. The three-electrode cell consisted of the AVAC as the working electrode, platinum (Pt) (1×1 cm^2) as the counter electrode, and Ag/AgCl as the reference electrode in 1 M KOH. The cyclic voltammo-grams (CVs) at different potential windows varying from −1 to 1 V were recorded at a scan rate of 10 mV s^{-1}. The obtained CV profiles are shown in Fig. 5(a). The optimum potential window seems to be from −1 to 0.2 V. Then, the CV profiles at different scan rates of 5, 10, 20, 30, 50, and 100 mV s^{-1} were recorded at a potential ranging from −1 to 0.2 V. The obtained CV profiles are shown in Fig. 5(b). From the CV profiles, it is clear that the profiles are quasi-rectangular in shape, implying the charge storage was primarily by the double layer formation. Even at higher scan rates, the CV profiles are nearly rectangular with a
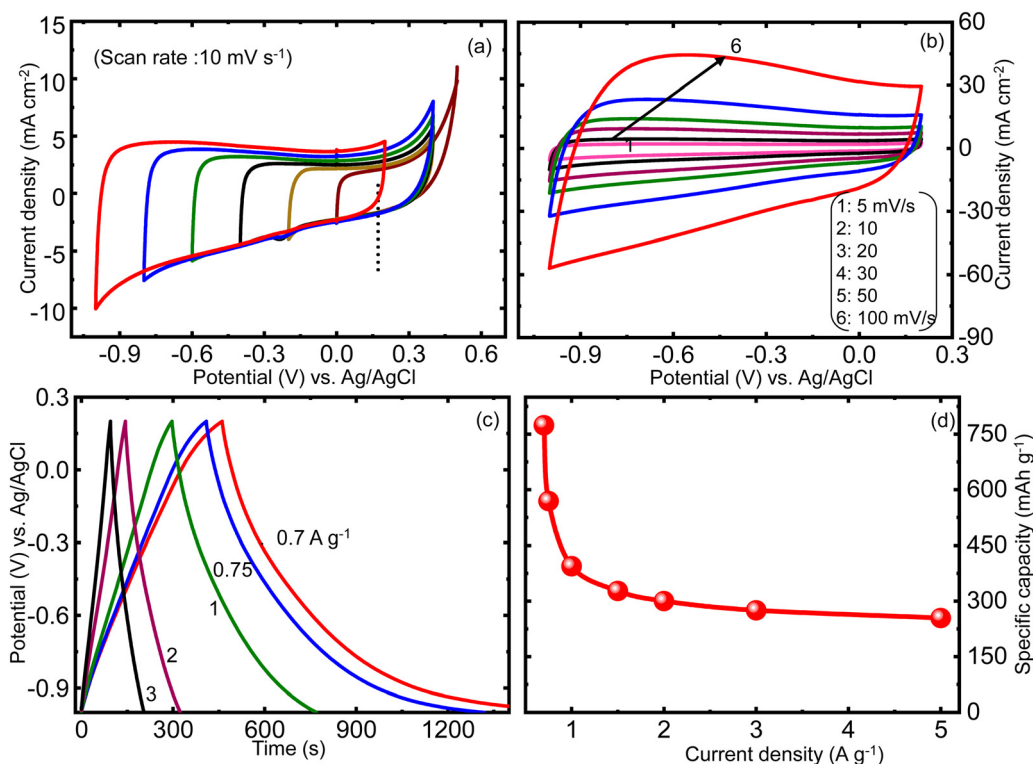

Fig. 5 (a) Cyclic voltammograms at different potential windows at a scan rate of 10 mV s^{-1}, (b) cyclic voltammograms at different scan rates, (c) galvanostatic charge–discharge profiles at different currents, and (d) dependence of specific capacitance on the current densities recorded for the AVAC electrode in 1 M KOH in a three electrode cell.

high current response, indicating the excellent reversibility of the material. To further examine the charge storage features of the AVAC electrode, galvanostatic charge–discharge (GCD) studies were performed. Fig. 5(c) shows the GCD curves recorded at different current densities of 0.7, 0.75, 1.0, 2.0 and 3.0 A g^{-1} in the potential from −1 to 0.2 V. It can be seen that the GCD curves are almost symmetrical at all the examined current densities, indicating a perfect double layer capacitor exhibited by the AVAC electrode. The GCD observations are consistent with the CV results discussed above. To quantify the stored charge, the specific capacitance was calculated from the discharge times using the formula given below:

$$Csp = \frac{I \times t}{V \times m} \, F \, g^{-1} \qquad (3)$$

where, Csp is the specific capacitance (F g^{-1}), I is discharge current (A), t is discharge time (s), V is the potential range (V) and m is the active mass of the electrode (g). Fig. 5(d) shows the specific capacitance obtained at different current densities. The AVAC electrode exhibits high specific capacitance.

Even at a high current density of 1 A g^{-1}, the specific capacitance was as high as 394 F g^{-1}. It is seen that as the current density increases, the specific capacitance decreases, which may be attributed to the limited utilization of the active material surface at higher current densities.

The total capacitance that is stored in an electrode is mainly due to the surface capacitive phenomenon and diffusion-controlled capacitive processes. The surface capacitive phenomenon involves the faradaic contribution from the pseudocapacitance caused by surface redox reactions and the non-faradaic contribution from the electrical double-layer formation. In diffusion-controlled capacitive processes, the diffusion of the ions into the bulk of an electrode plays a major role rather than the surface phenomenon.[27] In the present work, standard methods are used to deconvolute the surface capacitive, and the diffusive mode of charge contributes to the total capacitance. These are Dunn's and Trasatti's methods.

As per Dunn's method, the current response in a CV profile at a specific potential for a particular scan rate can be expressed as a sum of capacitive current and diffusive current, as shown below:

$$I\,(V) = k_1\nu + k_2\nu^{\frac{1}{2}} \qquad (4)$$

Or equivalently,

$$\frac{i\,(V)}{\nu^{1/2}} = k_1\nu^{1/2} + k_2 \qquad (5)$$

where, the first term of eqn (4), ($k_1\nu$) represents the capacitive contribution, and the second term, $k_2\nu^{1/2}$ diffusive contribution and $I\,(V)$ is the total current measured at a particular potential (V) in the CV profile.[28–30] Thus, a linear plot known as Dunn's plot was constructed by plotting $\frac{i\,(V)}{\nu^{1/2}}$ vs ($\nu^{1/2}$) as per eqn (5). As shown in Fig. 6, the slope (k_1) and y-intercept (k_2) of Dunn's plot were then obtained. From the values of k_1 and k_2, the absolute and percentage surface capacitive and diffusive contributions to the total capacitance of the AVAC electrode were estimated at

different scan rates and are shown in the form of bar diagrams in Fig. 6(c). The contributions of the surface capacitance to the total capacitance in the CV profiles recorded at a representative scan rate of 5 mV s^{-1} of the AVAC electrode are shown in Fig. 6(b). The contribution of the other scan rates of the electrode is given in Fig. S1 (ESI†). Thus, from the three electrode data, it is confirmed that the AVAC is a potential material for charge storage and is suitable for practical applications. The AVAC electrode has significant charge storage by means of a diffusive mode of charge flux, in particular at low scan rates. As given in the supplementary, the deconvolution by Dunn's approach revealed diffusive-charge storage of 34.01%. Such a diffusive mode of charge storage seems to be facilitated by the presence of heteroatoms in the explored mesoporous carbon. These heteroatoms would have facilitated diffusive processes such as electrosorption, and intercalation leading to the improved the capacitance of the AVAC electrode.
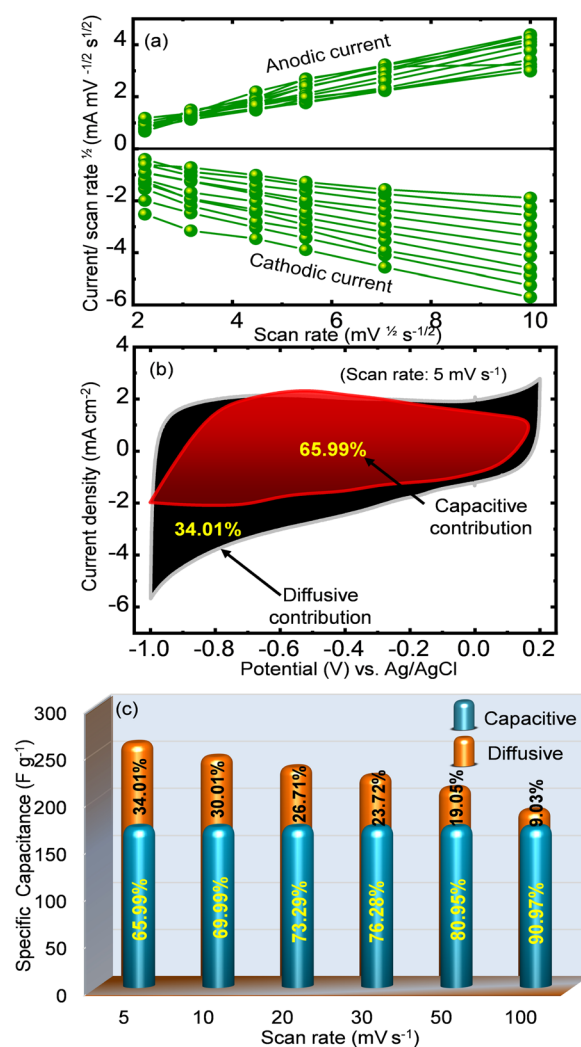

Fig. 6   (a) Linear plots of peak current vs. square root of the scan rate for the cathodic and anodic sweep at different potentials (b) deconvoluted CV profile at a scan rate of 5 mV s^{-1} marked with capacitive and diffusive contribution percentages and (c) percentages capacitive and diffusive contributions obtained by Dunn's method for the AVAC electrode.
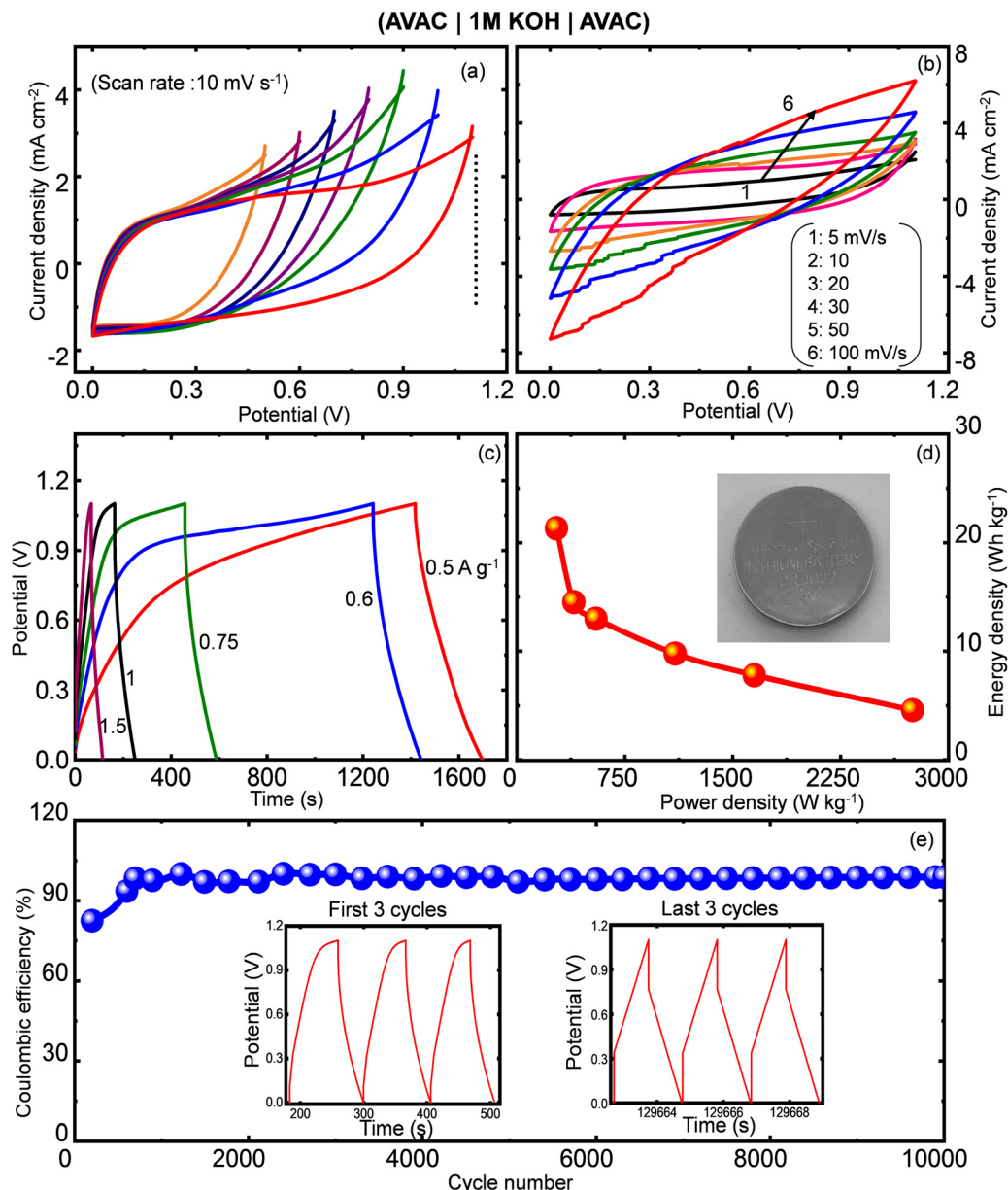
Fig. 7 (a) CV profiles recorded at different potential windows at a scan rate of 10 mV s^{-1}, (b) cyclic voltammograms at different scan rates, (c) GCD curves at different current densities, (d) Ragone plot, and (e) cycle-life data at 2 A g^{-1} recorded for the aqueous supercapacitor (AVAC|1 M KOH|AVAC) in the CR–2032 coin cell. Inset: Charge–discharge profiles of the first three and last three cycles.

3.2. Aqueous supercapacitor (AVAC|1 M KOH|AVAC) performances

As the three-electrode cell data confirmed, the excellent charge storage features of the AVAC electrode and its device performances were examined using a laboratory prototype aqueous supercapacitor. Thus, an aqueous supercapacitor in the form of a laboratory prototype CR–2032 coin cell having the AVAC as both the positive and negative electrodes, was fabricated in 1 M KOH electrolyte using Whatmann filter paper as the separator. Then, the CV profiles at different potential windows were recorded and the obtained profiles are shown in Fig. 7(a). The potential window suitable for the practical application seems to be in the range of 0–1.1 V. Further, detailed scan

rate-dependent CV profiles were recorded in the potential range of 0–1.1 V. The obtained CV profiles shown in Fig. 7(b) indicate a clear double-layer capacitance contribution in the aqueous supercapacitor device. It is seen that, as the scan rate increases, the current response in both anodic and cathodic regions also increases, showing the excellent reversibility of the device. Further, the GCD curves were recorded for the aqueous symmetric device at different current densities of 0.5, 0.6, 0.75, 1.0, and 1.5 A g^{-1}. The obtained profiles are shown in Fig. 7(c). The GCD profiles were almost symmetrical at each examined current density, confirming suitability for charge storage and release. The GCD results are consistent with the CV results discussed above. However, the charging time is a little higher than the

Table 1 Comparison of the potential window, the specific energy, and the specific power reported for the biomass-derived-carbon-based super-capacitor device in aqueous electrolyte and the present work

| Type of electrolyte	Source	Potential window (V)	Specific energy (W h kg^{-1})	Specific power (W kg^{-1})	Ref.
6 M KOH	Carrot	0–1.4	13.3	70	31
6 M KOH	Lettuce	0–1	7.4	50.4	36
6 M KOH	Willow catkin doped with N, S	0–1.8	21.0	180	37
1 M Na$_2$SO$_4$	Pines cones	0–2	19	∼100	32
1 M KOH	Avocado seed biomass-derived carbon	0–1.1	21	275	**This work**

discharging time, resulting in a low coulombic efficiency, which may be due to high electrode resistance and less utilization of the electrode active mass. From the discharge profiles, the specific energy and specific power of the AVAC-based symmetric device were calculated using the formulae following:[31]

$$E = CV^2/7.2 \text{ W h kg}^{-1} \quad (6)$$

$$P = 3600 \, E/t \text{ W kg}^{-1} \quad (7)$$

where, E is the specific energy (W h kg^{-1}), C is the specific capacitance (F g^{-1}), V is the potential range (V), P is the specific power (W kg^{-1}) and t is the discharge time (s). Fig. 7(d) shows the obtained Ragone for the aqueous device (AVAC|1 M KOH| AVAC). The AVAC-based aqueous supercapacitor exhibits a high specific energy of 21 W h kg^{-1} at a specific power of 275 W kg^{-1}. The specific energy of 4.5 W h kg^{-1} was observed even at a high specific power 2750 W kg^{-1}. Table 1 shows the comparison of the specific energy and the specific power reported for the various

biomass-derived activated carbon electrodes and the present value. The specific energy and the specific power observed in the present work are higher than most of the reported values.[32,33] Cycling stability is a prime factor to be considered for a practical device. Hence, cycle life analysis was performed on the fabricated aqueous device for 10 000 charge–discharge cycles at a current density of 2 A g^{-1}. The obtained data are displayed in Fig. 7(e). The cycling stability remained at almost 99% of the initial capacitance even at the 10 000th cycle, indicating the excellent stability of the device. The insets in Fig. 7(e) show the GCD profiles of the device recorded at the initial three and final three cycles. It is seen that there is a decrease in the charge/discharge times upon cycling. Usually upon cycling, the solution resistance and electrode resistance increase due to a decrease in the electrolyte conductivity and electrode degradation. The degradation is large if the electrode is other than carbon. Generally, the carbon electrodes show less degradation as there is no change in the composition or phase. However, the surface area and pore size
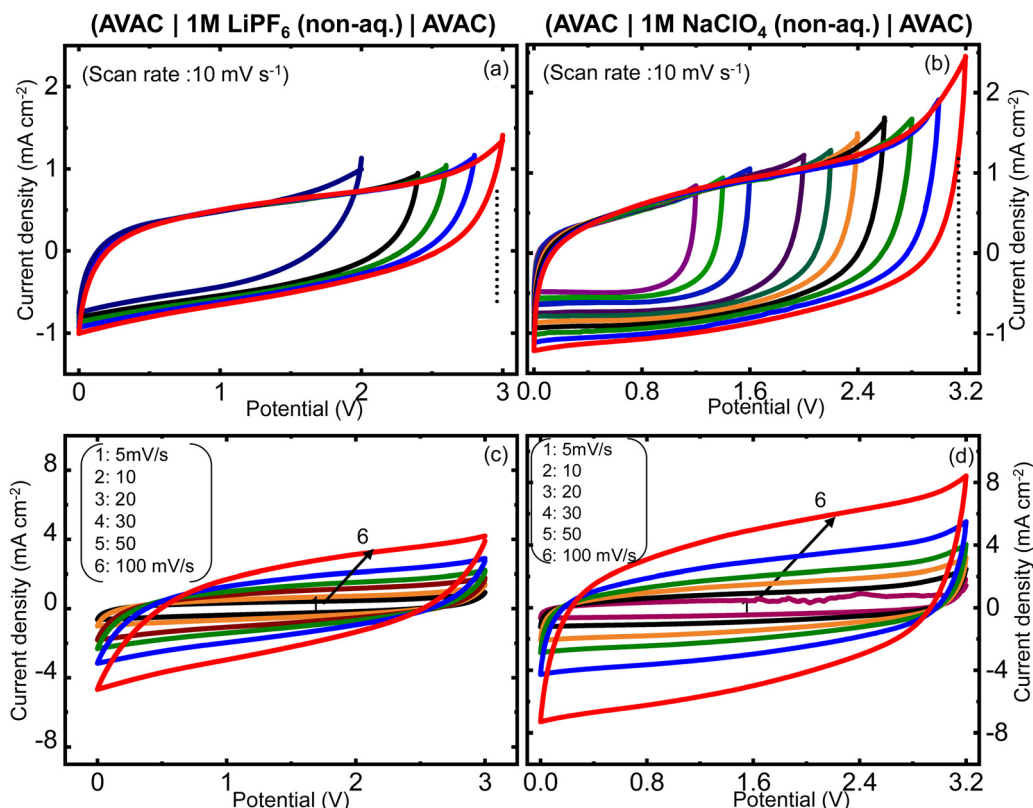
Fig. 8 (a and b) CV curves at different potential windows at a scan rate of 10 mV s^{-1} and (c and d) cyclic voltammograms at different scan rates for the dual carbon lithium-ion capacitor (left) and dual carbon sodium-ion capacitor (right) devices in the CR-2032 coin cell.
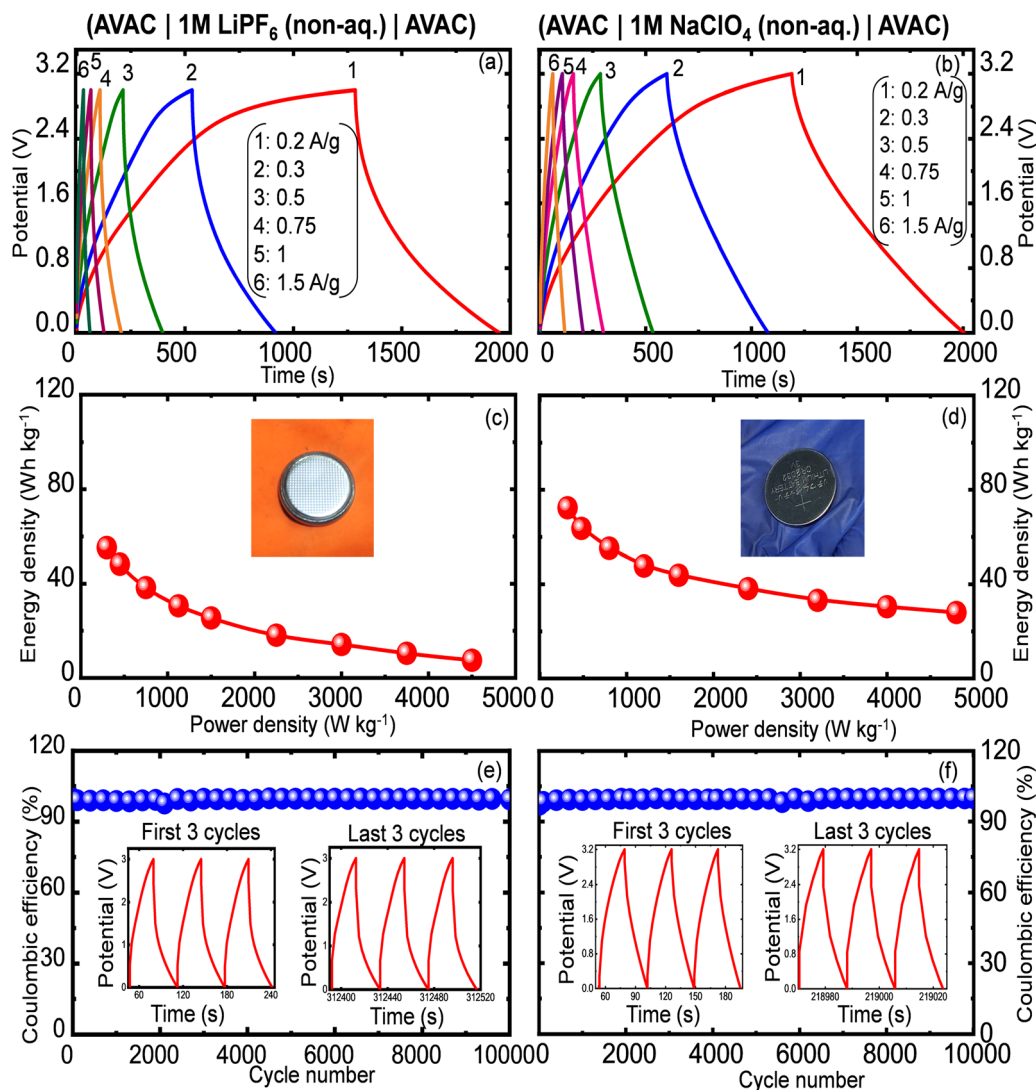
Fig. 9 (a and b) GCD curves at different currents densities for dual carbon lithium-ion capacitor (left) and dual carbon sodium-ion capacitor (right) devices in the CR-2032 coin cell, (c and d) Ragone plots and (e and f) Cycle life data of dual carbon lithium-ion capacitor (left) and dual carbon sodium-ion capacitor (right) in the CR-2032 coin cells in devices. Inset: First three and last three cycle charge−discharge profiles.

may change upon cycling. This might have led to increased resistance and resulted in a difference in the GCD profiles of the initial three and final three cycles.

3.3. Performance of dual carbon lithium-ion (AVAC|LiPF₆|AVAC) and sodium-ion (AVAC|NaClO₄|AVAC) supercapacitors

Though the AVAC electrode exhibited good performances in an aqueous electrolyte, as discussed in the previous section, the aqueous electrolytes are restricted to a limited operating potential of up to 1.2 V only. Moving to non-aqueous electrolytes can offer the great advantage of extending the operating potential to as high as 3 V. The high operating voltage of the device would result in enhanced specific energy, which is highly desirable. Hence, dual carbon lithium-ion capacitor (DC-LIC) and sodium-ion capacitor (DC-NIC) devices were fabricated using AVAC as both positive and negative electrodes in the

organic solvent containing lithium salt and sodium salt, respectively. The DC-LIC (AVAC|1 M LiPF₆ (non-aq)|AVAC) and DC-NIC (AVAC|1 M NaClO₄ (non-aq)|AVAC) were fabricated in the form of a laboratory prototype, CR-2032 coin cells. Then, the performances of the DC-LIC and the DC-NIC devices were examined using CV and GCD studies. The potential window of each device was optimized by recording cyclic voltammograms in different voltage windows at a fixed scan rate of 10 mV s⁻¹. The recorded CV profiles are shown in Fig. 8(a and b). It is observed that the optimized potential window could be 0–3 V for the DC-LIC, whereas, in the case of the DC-NIC, the potential window can be as high as 0–3.2 V. Beyond these voltage limits, it is unsafe as it would result in the decomposition of the electrolyte. Then, CV profiles at fixed potential windows, 0–3 V for the DC-LIC and 0–3.2 V for DC-NIC at different scan rates of 5, 10, 20, 30, 50, and 100 mV s⁻¹, were recorded. The obtained CV profiles are shown in Fig. 8(c and d).

Table 2 Comparison of the potential window, specific energy, and specific power of lithium-ion and sodium-ion capacitors reported in the literature with present work in non-aqueous electrolytes

| Type of capacitor	Source	Potential window (V)	Specific energy (W h kg^{-1})	Specific power (W kg^{-1})	Ref.
DC-LIC	Microporous carbide-derived carbon	0–3.2	36.7	83.6	38
	B,N doped carbon nanofiber	0.02–4.5	220	225	39
	Sorghum core derived carbon sheets	0–4.3	124.8	107	40
	Avocado seed biomass-derived carbon	**0–3**	**55.25**	**300**	**This work**
DC-NIC	Graphitic mesocarbon	1–4	93.5	573	41
	Carbon from cocoons	0.5–4	110	245	42
	Fruit juice derived carbon	2–4	52.2	300	43
	Avocado seed biomass-derived carbon	**0–3.2**	**72.36**	**320**	**This work**
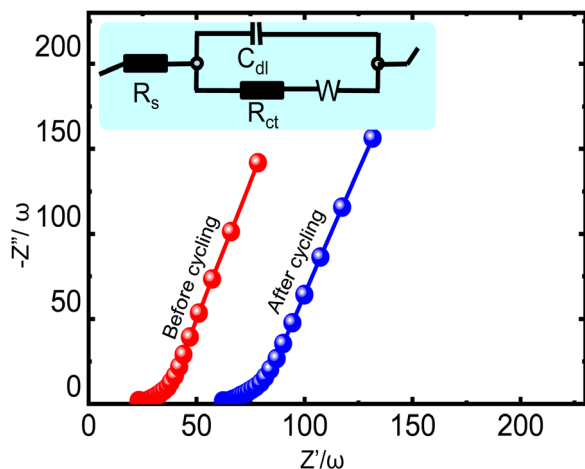
Fig. 10 Nyquist plots recorded for the dual carbon sodium-ion capacitor before, and after cycle life. Inset: Equivalent circuit used for fitting the Nyquist plot.

Table 3 Comparison of electrochemical impedance (EIS) data before cycle life and after cycle life in Sodium-ion capacitor (DC-NIC)

Cycle	R_s (Ω)	R_{ct} (Ω)	C (F)	W (Ω s$^{-1/2}$)
Before cycle	21.08	3.767	3.89×10^{-6}	40.9
After cycle	1000	100	0.1×10^{-6}	1

It is observed that the CV profiles are of quasi rectangle shape without any prominent redox peaks, indicating the charge storage is primarily by the double layer formation. The current response at different scan rates is high for DC-NIC compared to that obtained for DC-LIC, which indicates that the former is capable of higher charge storage than the latter. Even at high scan rates, the CV profiles were almost rectangular in shape with huge hysteresis, indicating high reversibility and excellent rate capability.

Fig. 9(a and b) shows the GCD curves of DC-LIC and the DC-NIC devices at different current densities, such as 0.2, 0.3, 0.5, 0.75, 1.0, and 1.5 A g^{-1}. It is important to note that there is a slight variation in the charge–discharge profiles of DC-LIC and DC-NIC. In the case of DC-LIC, the operating voltage could not be beyond 3 V as the saturation limit of the device voltage was attained due to the no more Li^{+} ion adsorption. Interestingly, in the case of the DC-NIC device, the upper potential limit can be up to 3.2 V. From the GCD profiles, Ragone plots were constructed and are depicted in Fig. 9(c and d). The specific energy and the specific power of both devices were calculated using eqn (6) and (7). The DC-LIC exhibited a specific energy of 55.25 W h kg^{-1} at a specific power of 300 W kg^{-1} and a specific energy of 25.4 W h kg^{-1} at a high specific power of 1500 W kg^{-1}, whereas, the DC-NIC exhibited a high specific energy of 72.36 W h kg^{-1} at a specific power of 320 W kg^{-1}, and a specific energy of 43.82 W h kg^{-1} at a specific power of 1600 W kg^{-1}. It should be noted that in the case of DC-LIC, the operating voltage could not be beyond 3 V during charging, as the device reached a saturation voltage due to no more Li^{+} ion electrosorption or intercalation, whereas, in the case of the DC-NIC, the operating voltage could be 3.2 V. This is because due to the large size of Na^{+}, there was less Na^{+} ion uptake at 3 V compared to the uptake of Li^{+} ion, hence, the operating voltage could be as high as 3.2 V. As the operating voltage is high, the DC-NIC resulted in high specific energy. The size-dependent operating voltage saturation was reported by Ling *et al.*[34] Table 2 shows the comparison of the specific energy and the specific power reported in the literature and this work. The specific energy and the specific power obtained in this work are higher than those in most of the studies reported in the
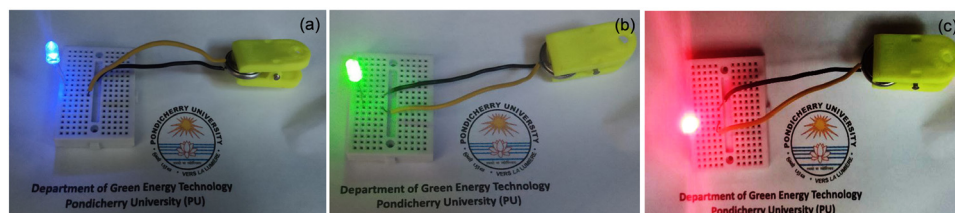
Fig. 11 Photographs of glowing blue (a), green (b), and red (c) LED bulbs powered by the dual carbon sodium–ion capacitor that contained AVAC carbon.

literature, implying that the developed avocado seed biomass-derived carbon is a potential material for practical use. Then, the fabricated devices were subjected to cycle life studies for 10 000 charge–discharge cycles at a current density of 1 A g^{-1} for the DC-LIC and 3 A g^{-1} for the DC-NIC device. The obtained cycle-life data are shown in Fig. 9(e and f). It is observed that the coulombic efficiency of both devices is nearly 100%. The charge–discharge curves recorded at the first three cycles and last three cycles are almost similar, affirming the stable charge retention and coulombic efficiency of the device.

To examine the ion and electron transports, electrochemical impedance spectroscopy (EIS) studies were performed on the DC-NIC device before and after conducting the cycle life. The EIS studies were performed in the frequency range of 100 kHz–0.01 Hz. Fig. 10 shows the obtained Nyquist plots. It can be seen that the Nyquist plots consisted of a small semicircle at a high-frequency region and a spike 45° inclined to the x-axis. The presence of the spike 45° inclined to the x-axis is characteristic of a capacitor. The Nyquist plots obtained could be the best fit with the Randles circuit shown in the inset of Fig. 10. The equivalent circuit consists of a solution resistance (R_s), charge transfer resistance (R_{ct}), and capacitance in parallel with the Warburg component. The obtained fit values are shown in Table 3. Upon cycling, the electrode/electrolyte resistance increased, which may be due to the degradation of the electrode, which is pertinent at high cycles, as has been reported.[35]

Further, the fabricated DC-NIC device was used for the practical demonstration by powering each red, blue, and green color commercial LED bulbs. Fig. 11 shows the photographs of the commercial LED bulbs being powered by the DC-NIC device. It was found that once charged, the coin cell could charge the green LED bulb for about 16 min.

4. Conclusions

The avocado seed biomass-derived activated carbon was successfully synthesized by pyrolysis followed by chemical activation using KOH. The resulting bio-carbon was confirmed to exhibit a specific energy of 21 W h kg^{-1} at the specific power of 275 W kg^{-1} in an aqueous electrolyte with excellent cycling stability. For the first time, a dual carbon sodium-ion capacitor (DC-NIC) was fabricated using the avocado seed-derived carbon (AVAC) that exhibited an outstanding specific energy of 72.36 W h kg^{-1} at a specific power of 320 W kg^{-1} with almost 100% coulombic efficiency even at 10 000th cycle, while the dual carbon lithium-ion capacitor (DC-LIC) device exhibited high specific energy of 55.25 W h kg^{-1} at a specific power of 300 W kg^{-1} with nearly 100% coulombic efficiency. The fabricated DC-NIC coin cell prototype device was demonstrated to power red, blue, and green commercial LED bulbs. The once-charged DC-NIC coin cell device could power the green LED bulb for almost 16 min. Thus, the synthesized and tested avocado seed biomass-derived carbon can be a good candidate for both aqueous and non-aqueous supercapacitor applications.

The biomass source used is widely available and the method adopted is feasible, and can be scaled up.

Conflicts of interest

There are no conflicts of interest to declare.

Acknowledgements

References

1 M. Höök and X. Tang, Depletion of fossil fuels and anthropogenic climate change-A review, *Energy Policy*, 2013, **52**, 797–809.

2 R. A. Mir, S. Upadhyay, R. A. Rather, S. J. Thorpe and O. P. Pandey, Single-step in situ synthesis of MoO2-faceted structures as highly efficient HER electrocatalysts and electrode materials for pseudocapacitors, *Energy Adv.*, 2022, **1**, 438–448.

3 P. Asantewaa Owusu and S. Asumadu-Sarkodie, A review of renewable energy sources, sustainability issues and climate change mitigation, *Cogent Eng.*, 2016, **3**, 1167990.

4 Y. Zheng, H. Wang, S. Sun, G. Lu, H. Liu, M. Huang, J. Shi, W. Liu and H. Li, Sustainable nitrogen-doped carbon electrodes for use in high-performance supercapacitors and Li-ion capacitors, *RSC Sustainable Energy Fuels*, 2020, **4**, 1789.

5 T. Maiyalagan and P. Elumalai, *Rechargeable Lithium-ion Batteries: Trends and Progress in Electric Vehicles*, CRC Press, 2020, DOI: , DOI: **10.1201/9781351052702**.

6 K. Sarode and S. Martha, Li$_{1.2}$Mn$_{0.55}$Ni$_{0.15}$Co$_{0.1}$O$_2$(LMR-NMC)-Carbon Coated-LiMnPO$_4$ Blended Electrodes for High Performance Lithium Ion Batteries, *J. Electrochem. Soc.*, 2018, **165**, A463–A468.

7 S. Saini, P. Chand and A. Joshi, Biomass derived carbon for supercapacitor applications: Review, *J. Energy Storage*, 2021, **39**, 102646.

8 A. Kumar, G. Ahmed, M. Gupta, P. Bocchetta, R. Adalati, R. Chandra and Y. Kumar, Theories and models of supercapacitors with recent advancements: impact and interpretations, *Nano Express*, 2021, **2**, 022004.

9 H. Wang, C. Zhu, D. Chao, Q. Yan and H. J. Fan, Nonaqueous Hybrid Lithium-Ion and Sodium-Ion Capacitors, *Adv. Mater.*, 2017, **29**, 1702093.

10 D. Stepien, Z. Zhao and S. Dsoke, Shift to Post-Li-Ion Capacitors: Electrochemical Behavior of Activated Carbon Electrodes in Li-, Na- and K-Salt Containing Organic Electrolytes, *J. Electrochem. Soc.*, 2018, **165**, A2807–A2814.

11 X. Wang, L. Liu and Z. Niu, Carbon-based materials for lithium-ion capacitors, *Mater. Chem. Front.*, 2019, **3**, 1265.

12 J. Ajuria, M. Zarrabeitia, M. Arnaiz, O. Urra, T. Rojo and E. Goikolea, Graphene-coffee waste derived carbon composites as electrodes for optimized lithium ion capacitors, *J. Electrochem. Soc.*, 2019, **166**, A2840–A2848.

13 W. Qian, F. Sun, Y. Xu, L. Qiu, C. Liu, S. Wang and F. Yan, Human hair-derived carbon flakes for electrochemical supercapacitors, *Energy Environ. Sci.*, 2014, **7**, 379–386.

14 T. Kesavan, T. Partheeban, M. Vivekanantha, M. Kundu, G. Maduraiveeran and M. Sasidharan, Microporous and Mesoporous Materials Hierarchical nanoporous activated carbon as potential electrode materials for high performance electrochemical supercapacitor, *Microporous Mesoporous Mater.*, 2019, **274**, 236–244.

15 K. Subramanyan, M. L. Divya and V. Aravindan, Dual-carbon Na-ion capacitors: progress and future prospects, *J. Mater. Chem. A*, 2021, **9**, 9431–9450.

16 B. Wang, X. Gao, L. Xu, K. Zou, P. Cai, X. Deng, L. Yang, H. Hou, G. Zou and X. Ji, Advanced Carbon Materials for Sodium-Ion Capacitors, *Batteries Supercaps*, 2021, **4**, 538–553.

17 H. Wang, D. Mitlin, J. Ding, Z. Li and K. Cui, Excellent energy-power characteristics from a hybrid sodium ion capacitor based on identical carbon nanosheets in both electrodes, *J. Mater. Chem. A*, 2016, **4**, 5149.

18 M. Vadivazhagan, P. Packiyalakshmi, M. Ulaganathan and K. Nallathamby, Waste-Driven Bio-Carbon Electrode Material for Na-Ion Storage Applications, *ACS Sustainable Chem. Eng.*, 2018, **6**, 13915–13923.

19 L. Yin, J. Feng and X. Zhang, Materials Advanced sodium-ion pseudocapacitor performance of oxygen-implanted hard carbon derived from carbon spheres, *J. Mater. Sci.*, 2019, **54**, 4124–4134.

20 F. Tuinstra and J. L. Koenig, Characterization of Graphite Fiber Surfaces with Raman Spectroscopy, *J. Compos. Mater.*, 1970, **4**, 492–499.

21 M. A. Pimenta, G. Dresselhaus, M. S. Dresselhaus, L. G. Cançado, A. Jorio and R. Saito, Studying disorder in graphite-based systems by Raman spectroscopy, *Phys. Chem. Chem. Phys.*, 2007, **9**, 1276–1291.

22 N. Kumar, S. Das, C. Bernhard and G. D. Varma, Effect of graphene oxide doping on superconducting properties of bulk MgB_2, *Supercond. Sci. Technol.*, 2013, **26**, 095008.

23 H. Ding, J.-S. Wei and H.-M. Xiong, Nitrogen and sulfur co-doped carbon dots with strong blue luminescence, *Nanoscale*, 2014, **6**, 13817.

24 R. Chulliyote, H. Hareendrakrishnakumar, M. Raja, M. Gladis and A. Stephan, Sulfur-Immobilized Nitrogen and Oxygen Co–Doped Hierarchically Porous Biomass Carbon for Lithium-Sulfur Batteries: Influence of Sulfur Content and Distribution on Its Performance, *ChemistrySelect*, 2017, **2**, 10484–10495.

25 P. Yan, H. Ye, Y. Han, J. Wang, F. Zheng, W. Xiong, H. Yang, J. Zhang, A. Yuan and X. Wu, Dual-Templating Approaches to Soybeans Milk-Derived Hierarchically Porous Heteroatom-Doped Carbon Materials for Lithium-Ion Batteries, *ChemistryOpen*, 2020, **9**, 582–587.

26 L. Zhang, L. Xu, Y. Zhang, X. Zhou, L. Zhang, A. Yasin, L. Wang and K. Zhi, Facile synthesis of bio-based nitrogen and oxygen-doped porous carbon derived from cotton for supercapacitors, *RSC Adv.*, 2018, **8**, 3869–3877.

27 B. Babu and M. M. Shaijumon, High performance sodium-ion hybrid capacitor based on $Na_2Ti_2O_4(OH)_2$ nanostructures, *J. Power Sources*, 2017, **353**, 85–94.

28 J. Wang, J. Polleux, J. Lim and B. Dunn, Pseudocapacitive Contributions to Electrochemical Energy Storage in TiO_2 (Anatase) Nanoparticles, *J. Phys. Chem. C*, 2007, **111**, 14925–14931.

29 S. Liu, J. Yang, X. Song, Y. Wang, W. Zhang and M. Chhowalla, Microwave-Reduced Graphene Oxide for Aluminum Batteries, *ACS Appl. Nano Mater.*, 2022, **5**, 14347–14355.

30 T. Panja, J. Ajuria, N. Diez, D. Bhattacharjya, E. Goikolea and D. Carriazo, Fabrication of high-performance dual carbon Li-ion hybrid capacitor: mass balancing approach to improve the energy-power density and cycle life, *Sci. Rep.*, 2020, **10**, 10842.

31 E. Sujithkrishnan, A. Prasath, M. Govindasamy, R. A. Alshgari and P. Elumalai, Pyrrolic-Nitrogen-Containing Hierarchical Porous Biocarbon for Enhanced Sodium-Ion Energy Storage, *Energy Fuels*, 2021, **35**, 5320–5332.

32 J. Liu, S. Min, F. Wang and Z. Zhang, Biomass-derived three-dimensional porous carbon membrane electrode for high-performance aqueous supercapacitors: An alternative of powdery carbon materials, *J. Power Sources*, 2020, **466**, 228347.

33 A. Bello, N. Manyala, F. Barzegar, A. A. Khaleed, D. Y. Momodu and J. K. Dangbegnon, Renewable pine cone biomass derived carbon materials for supercapacitor application, *RSC Adv.*, 2016, **6**, 1800.

34 C. Ling, J. Chen and F. Mizuno, First-Principles Study of Alkali and Alkaline Earth Ion Intercalation in Iron Hexacyanoferrate: The Important Role of Ionic Radius, *J. Phys. Chem. C*, 2013, **117**, 21158–21165.

35 S. Archana, M. Athika and P. Elumalai, Supercapattery and full-cell lithium-ion battery performances of a [Ni(Schiff base)]-derived Ni/NiO/nitrogen-doped carbon heterostructure, *New J. Chem.*, 2020, **44**, 12452–12464.

36 J. Liu, S. Min, F. Wang and Z. Zhang, High-Performance Aqueous Supercapacitors Based on Biomass-Derived Multi-heteroatom Self-Doped Porous Carbon Membranes, *Energy Technol.*, 2020, **8**, 2000391.

37 Y. Li, G. Wang, T. Wei, Z. Fan and P. Yan, Nitrogen and sulfur co-doped porous carbon nanosheets derived from willow catkin for supercapacitors, *Nano Energy*, 2016, **19**, 165–175.

38 A. Laheäär, H. Kurig, A. Jänes and E. Lust, $LiPF_6$ based ethylene carbonate–dimethyl carbonate electrolyte for high power density electrical double layer capacitor, *Electrochim. Acta*, 2009, **54**, 4587–4594.

39 Q. Xia, H. Yang, M. Wang, M. Yang, Q. Guo, L. Wan, H. Xia and Y. Yu, High Energy and High Power Lithium-Ion Capacitors Based on Boron and Nitrogen Dual-Doped 3D Carbon Nanofibers as Both Cathode and Anode, *Adv. Energy Mater.*, 2017, **7**, 1–9.

40 X. Xu, Y. Cui, J. Shi, W. Liu, S. Chen, X. Wang and H. Wang, Sorghum core-derived carbon sheets as electrodes for a lithium-ion capacitor, *RSC Adv.*, 2017, **7**, 17178.

41 P. Han, X. Han, J. Yao, L. Zhang, X. Cao, C. Huang and G. Cui, High energy density sodium-ion capacitors through co-intercalation mechanism in diglyme-based electrolyte system, *J. Power Sources*, 2015, **297**, 457–463.

42 Y. S. Yun, Y. Cho, H. Kim, H. J. Jin and K. Kang, Ultra-Thin Hollow Carbon Nanospheres for Pseudocapacitive Sodium-Ion Storage, *ChemElectroChem*, 2014, **2**, 359–365.

43 S. Wang, R. Wang, Y. Zhang, D. Jin and L. Zhang, Scalable and sustainable synthesis of carbon microspheres via a purification-free strategy for sodium-ion capacitors, *J. Power Sources*, 2018, **379**, 33–40.